Seasonal Superrotation in Earth's Troposphere

PENGCHENG ZHANG[a] AND NICHOLAS J. LUTSKO[a]

[a] *Scripps Institution of Oceanography, University of California, San Diego, La Jolla, California*

(Manuscript received 13 March 2022, in final form 21 August 2022)

ABSTRACT: Although Earth's troposphere does not superrotate in the annual mean, for most of the year—from October to May—the winds of the tropical upper troposphere are westerly. We investigate this seasonal superrotation using reanalysis data and a single-layer model for the winds of the tropical upper troposphere. We characterize the temporal and spatial structures of the tropospheric superrotation, and quantify the relationships between the superrotation and the leading modes of tropical interannual variability. We also find that the strength of the superrotation has remained roughly constant over the past few decades, despite the winds of the tropical upper troposphere decelerating (becoming more easterly) in other months. We analyze the monthly zonal-mean zonal momentum budget and use numerical simulations with an axisymmetric, single-layer model of the tropical upper troposphere to study the underlying dynamics of the seasonal superrotation. Momentum flux convergence by stationary eddies accelerates the superrotation, while cross-equatorial easterly momentum transport associated with the Hadley circulation decelerates the superrotation. The seasonal modulations of these two competing factors shape the superrotation. The single-layer model is able to qualitatively reproduce the seasonal progression of the winds in the tropical upper troposphere, and highlights the northward displacement of the intertropical convergence zone in the annual mean as a key factor responsible for the annual cycle of the tropical winds.

KEYWORDS: Stationary waves; Atmospheric circulation; Hadley circulation; Seasonal cycle; Upper troposphere

1. Introduction

Superrotation refers to a state in which an atmosphere has greater angular momentum than its planet's surface at the equator. That is, superrotation requires that the zonal-mean zonal wind U satisfies $U > U_m$, where

$$U_m = \Omega a \sin^2(\phi)/\cos\phi, \tag{1}$$

with Ω as the planet's rotation rate, a as the planet's radius, and ϕ as latitude. Superrotation usually manifests as westerly zonal-mean winds over the equator, as off-equatorial angular momentum maxima are inertially unstable (e.g., see Eliassen and Kleinschmidt 1957).

Atmospheric superrotation is seen in a wide variety of planetary contexts. The atmospheres of Venus (Belton et al. 1991; Peralta et al. 2007; Horinouchi et al. 2020) and Titan (Bird et al. 2005; Kostiuk et al. 2006) are observed to superrotate, while two of the gas giants in the solar system, Jupiter and Saturn, have superrotating atmospheres relative to the rotation of their magnetic fields (Seiff 2000; Genio et al. 2009; note that the concept of superrotation on gas giants is ambiguous because gas giants do not have a well-defined surface). Outside the solar system, the atmospheres of many tidally locked gas giants and terrestrial exoplanets are expected to superrotate (Showman and Polvani 2011; Tsai et al. 2014; Pierrehumbert and Hammond 2019), and on Earth superrotation has been linked to the possible "permanent El Niño–like" state of the tropical Pacific during the Pliocene (Tziperman and Farrell 2009) and also appears in simulations of extreme global warming scenarios (Caballero and Huber 2010; Laraia and Schneider 2015).

Hide's theorem says that superrotation must be maintained by upgradient angular momentum fluxes (Hide 1969, 1970; Gierasch 1975; Held and Hou 1980; Schneider 2006), which suggests that eddies must be involved for an atmosphere to achieve superrotation. One possible mechanism of eddy generation is stationary or propagating vorticity sources in the deep tropics. A number of studies have investigated superrotation associated with localized tropical heating, motivated in some cases by the dynamics of tidally locked exoplanets (Suarez and Duffy 1992; Saravanan 1993; Hoskins et al. 1999; Kraucunas and Hartmann 2005; Norton 2006; Adames and Wallace 2017; Caballero and Huber 2010; Showman and Polvani 2010; Arnold et al. 2012; Lutsko 2018; Herbert et al. 2020). The wave response to tropical heating is generally found to be similar to the classic Matsuno–Gill model (Matsuno 1966; Gill 1980), though Showman and Polvani (2010) demonstrated that vertical momentum exchange must be added to the Matsuno–Gill model in order for there to be net momentum convergence onto the equator. Showman and Polvani (2011) and Pinto and Mitchell (2016) further argued that equatorial waves are mostly trapped in the tropics, and so focused on the role of phase tilts due to differential zonal propagation of equatorial waves, rather than meridional propagation, for generating equatorward momentum fluxes.

Alternatively, eddies can be generated spontaneously in the deep tropics due to instabilities, without explicit tropical forcing. This has been seen in simulations of small and/or slowly rotating planets with axisymmetric thermal forcing, for which transient eddies converge momentum onto the equator and drive superrotation [see Wang and Mitchell (2014) and

---

Corresponding author: Pengcheng Zhang, pczhang@ucsd.edu

DOI: 10.1175/JAS-D-22-0066.1

Lewis et al. (2021) for the dependence of superrotation on planetary rotation rate]. Our understanding of the nature of the instabilities driving these transient eddies has evolved. Spontaneous superrotation was first attributed to classic barotropic instability (e.g., Williams 2003; Mitchell and Vallis 2010), whereas more recent literature (e.g., Potter et al. 2014; Wang and Mitchell 2014; Zurita-Gotor and Held 2018; Zurita-Gotor et al. 2022) has suggested the equatorial acceleration is due to an ageostrophic Rossby–Kelvin instability [see Sakai (1989) for a detailed description of the Rossby–Kelvin instability]. Equatorial superrotation can be further enhanced by a reduction in the breaking of baroclinic eddies originating in midlatitudes, which decelerates the flow in the tropics under Earthlike conditions (Laraia and Schneider 2015; Polichtchouk and Cho 2016).

On Earth, the stratosphere superrotates during the westerly phase of the quasi-biennial oscillation (QBO; see Baldwin et al. 2001), but the climatological winds of the troposphere do not superrotate. The reason for the lack of annual-mean superrotation was first identified by Lee (1999), who showed that the seasonal cycle of the Hadley circulation is crucial for decelerating the flow, as the cross-equatorial flow brings air with low angular momentum across the equator, especially during the solstitial seasons (see also Dima et al. 2005; Yang et al. 2013). Alternatively, we note that the annual-mean intertropical convergence zone (ITCZ) is located north of the equator and so, assuming that the strongest zonal-mean ascent occurs in the ITCZ, the dynamics of an angular momentum–conserving Hadley circulation require that the annual-mean zonal flow in the equatorial upper troposphere be easterly (see, e.g., Held and Hou 1980; Lindzen and Hou 1988; Hill et al. 2019). Although the observed Hadley circulation is not strictly angular momentum conserving, the hemispheric differences which cause the ITCZ to be located off the equator in the annual mean can also be said to prevent Earth's troposphere from superrotating.

Nevertheless, while Earth's tropical troposphere does not superrotate in the annual mean, it does superrotate on seasonal time scales. For example, Fig. 1 of Zurita-Gotor (2019) shows that the vertically integrated equatorial winds between 300 and 150 hPa superrotate from November to March.[1] By Hide's theorem, this means that eddies must be converging momentum onto the equator, and that this momentum convergence overcomes the deceleration by the mean flow, even during the winter solstice. Zurita-Gotor (2019) studied the mechanisms of meridional eddy momentum transport in the tropics in detail, but did not characterize the spatial and temporal structure of the seasonal tropospheric superrotation or investigate how the eddy momentum flux interacts with the other terms in the momentum budget.

The present study investigates the seasonal superrotation of Earth's tropical upper troposphere using a combination of reanalysis data and simple numerical simulations. We characterize the superrotation's structure in time and space, and examine its potential relationships with leading modes of tropical variability: superrotation is favored in La Niña years and during the easterly phase of the QBO. We identify stationary eddy momentum flux convergence as playing a crucial role in driving the superrotation, and are able to explain the seasonality of the superrotation using a simple numerical model. The eddy momentum flux convergence makes the superrotation possible during most of the year, while the strong cross-equatorial Hadley circulation prevents superrotation in boreal summer, producing the annual cycle of the upper-tropospheric winds seen today. It is the dynamic balance between these two factors that shapes the characteristics and the seasonality of the superrotation.

The remainder of this paper is structured as follows. Section 2 introduces the datasets and numerical model we use. Section 3 describes the main characteristics of the seasonal superrotation in Earth's tropical troposphere, including its structure, relationship with the major modes of interannual tropical variability, and recent trends. Section 4 analyzes the monthly mean zonal momentum budgets to identify the drivers of the superrotation and to explain why it is only present for part of the year. In section 5 we use a numerical model of the tropical upper troposphere to explore how various factors contribute to the seasonal superrotation and to confirm our interpretation of the momentum budget analysis. We end in section 6 with a summary and conclusions.

2. Methods

a. Data

Daily wind speed data are obtained by averaging 3-hourly assimilated meteorological fields product (GMAO 2015) from the Modern-Era Retrospective Analysis for Research and Applications, version 2 (MERRA-2; Gelaro et al. 2017). The data used in this study span the period 1980–2020 and pressure levels between 1000 and 10 hPa. MERRA-2 uses a horizontal resolution of 0.625° × 0.5°, while the vertical grid spacing is 50 hPa in the mid- and upper troposphere, which is the primary focus of this study.

To verify the robustness of the superrotation, we have repeated the analysis with three other reanalysis products: the European Centre for Medium-Range Weather Forecasts (ECMWF) Reanalysis v5 (ERA5; 0.25° × 0.25° resolution; Hersbach et al. 2020), the Japanese 55-year Reanalysis (JRA-55; 1.25° × 1.25° resolution; Kobayashi et al. 2015), and the National Centers for Environmental Prediction Reanalysis 1 (NCEP-1; 2.5° × 2.5° resolution; Kalnay et al. 1996). For all three reanalysis products, data are taken for the period 1980–2020, and the results are shown in appendix A.

To explore the relationship between the equatorial winds and El Niño–Southern Oscillation (ENSO), we use the oceanic Niño index (ONI; see NOAA 2021) published by the National Oceanic and Atmospheric Administration's (NOAA)[2]

---

[1] Interestingly, Dima et al. (2005) saw weak superrotation in October–November and April–May, but not in boreal winter. However, they used the older NCEP reanalysis, and below we confirm the superrotation in boreal winter using more recent reanalysis products.

[2] https://www.noaa.gov/.

TABLE 1. Model parameter values used in this study.

Parameter	Value	Definition
τ	37 days	Thermal relaxation time
H	16 km	Tropopause height
δ	4 km	Depth of layer
T_0	300 K	Reference surface temperature
Δ_z	60 K	Vertical potential temperature stratification
Δ_y	50 K	RE equator-to-pole temperature gradient
θ_{00}	330 K	Background tropospheric-mean potential temperature
ϵ_u	10^{-8} s^{-1}	Background Rayleigh drag
k_v	7.79×10^4 m^2 s^{-1}	Diffusivity
β	2×10^{-11} m^{-1} s^{-1}	Meridional gradient of Coriolis parameter
y_{am}	666 km	Latitude of the annual-mean ITCZ
$y_0(t)$	Varying	Subsolar latitudes
t_0	79	Spring equinox day in the year
y_M	2608 km	Subsolar latitude at equinoxes

Climate Prediction Center (CPC).[3] The ONI is based on the 3-month running mean of sea surface temperature (SST) anomalies in the Niño-3.4 region (5°N–5°S, 120°–170°W; see NOAA 2020). NOAA considers El Niño conditions to be present when the ONI is + 0.5 or higher, indicating the east-central tropical Pacific is significantly warmer than usual, and La Niña conditions to be present when the ONI is −0.5 or lower, indicating the region is cooler than usual (Dahlman 2016; NOAA 2021).

b. *Single-layer model*

We use an axisymmetric single-layer model adapted from Sobel and Schneider (2009) (see also Sobel and Schneider 2013) to reconstruct and understand the superrotation. This model was originally used to study interactions of the Hadley circulation with eddies, and is able to reproduce key qualitative features of the Hadley circulation in idealized GCM simulations. The model equations are

$$\partial_t u - v(\beta y - \partial_y u) = \mathscr{H}(\partial_y v)(\partial_y v)u - \mathscr{F} - \mathscr{S}, \tag{2}$$

$$2\partial_t v + \beta y u = -\frac{gH}{T_0}\partial_y T, \tag{3}$$

$$\partial_t \theta + \frac{\delta \Delta_z}{H}\partial_y v = \frac{\theta_E - \theta}{\tau}, \tag{4}$$

where u and v represent the zonal-mean zonal and meridional flow, respectively, in a thin layer below the tropopause of constant thickness δ at constant height H. Potential temperature θ and temperature T are related by $\theta = T(p_s/p_t)^{R/c_p}$ with fixed tropopause and surface pressures p_t and p_s such that the constant factor $(p_s/p_t)^{R/c_p} = 1.6$. Also set fixed are the potential temperature difference Δ_z between the surface and tropopause; the surface temperature T_0; and the thermal relaxation time τ. The radiative equilibrium (RE) temperature $\theta_E = \theta_E(y, t)$ is a prescribed function of latitude and time; $\mathscr{S}$ represents eddy momentum flux divergence (EMFD); and $\mathscr{F} = \epsilon_u u$ represents frictional drag. The first term on the rhs of Eq. (2) corresponds to vertical momentum advection, where $\mathscr{H}$ is the Heaviside function. Note that under the β-plane approximation, the y in this model is the distance from the equator in units of meters.

To generate a realistic seasonal cycle, we prescribe a thermal forcing which varies in time as

$$\theta_E = \begin{cases} \theta_{00} - \Delta_y \left[\dfrac{y - y_0(t) - y_{\mathrm{am}}}{y_1}\right]^2 & \text{if } |y| < y_1, \\ \theta_{00} - \Delta_y & \text{if } |y| \geq y_1, \end{cases} \tag{5}$$

where $y_1 = 9439$ km (~85° of latitude) and $y_0(t)$ is the subsolar latitude over the course of the annual cycle, which takes the form

$$y_0(t) = y_M \sin\left[\frac{2\pi}{t_a}(t - t_0)\right], \tag{6}$$

where $t_a = 365$ is the length of a year in days, $t_0 = 79$ is the spring equinox, and y_M is the subsolar latitude at the summer solstice, which we set to 2608 km (~23.5°N) and $y_{\mathrm{am}} = 666$ km (~6°N) denotes the latitude of the annual-mean ITCZ in today's climate. A complete list of parameter values is given in Table 1.

As in Sobel and Schneider (2009), the model is integrated on a staggered grid using a leapfrog time-stepping scheme. The domain contains 801 grid points for v and 800 grid points for u and θ, for a resolution of 39.3 km. A second-order diffusion term, though not explicitly shown in the equations, is also included to keep the model numerically stable. In all simulations, the model was integrated for 15 model years and we show averages over the last five years of the simulations.

3. Characterizing boreal winter superrotation

a. *Observed structure of the superrotation*

We begin by examining the spatial and temporal structure of the zonal winds near the equator. Plotting the climatological seasonal zonal-mean winds in the deep tropics clearly shows the presence of tropospheric superrotating winds in boreal

---

[3] https://www.cpc.ncep.noaa.gov/.

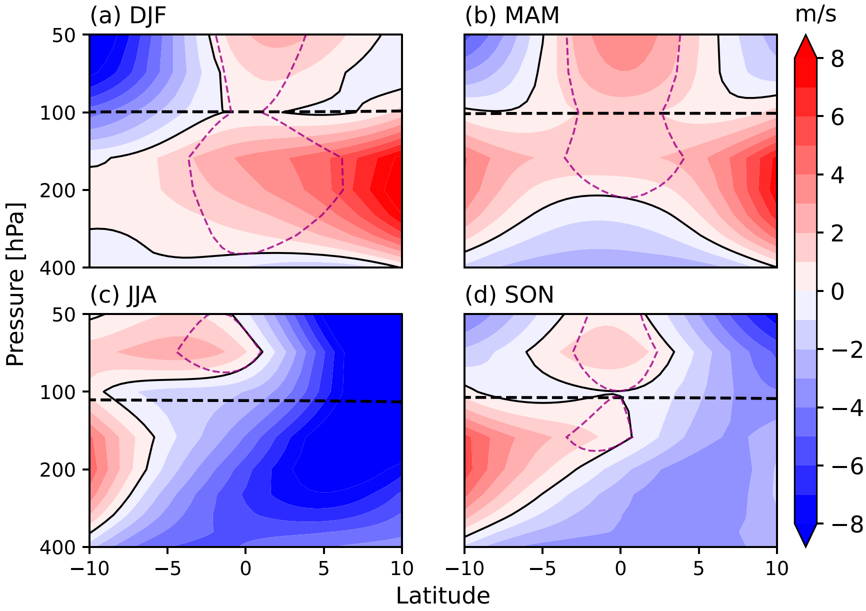

FIG. 1. Seasonality of the tropical zonal-mean zonal wind speeds at different latitudes and levels in MERRA-2. The shading denotes wind velocities, with a contour interval of 1 m s^{-1}. The black dashed lines denote the average height of the tropopause, defined as the lowest level at which the lapse rate decreases to 2 K km^{-1} or less. Regions where the wind speed is greater than or equal to the superrotating winds defined by Eq. (1) are enclosed by the purple dashed lines.

winter [December–February (DJF)], and also weak superrotation in March–May (MAM) and September–November (SON; see Figs. 1a,b,d). In DJF the winds over the equator are westerly between roughly 250 and 100 hPa, with a maximum speed of 4 m s^{-1} at 150 hPa. These westerly winds appear as an extension of the subtropical jet in the Northern Hemisphere, and the zonal winds strengthen moving northward from the equator. The weaker superrotation in MAM has a maximum wind speed of less than 2 m s^{-1} and is centered in a narrower band of the upper troposphere (~200–100 hPa). The zonal winds are more symmetric about the equator in MAM, and there are subtropical jets in both hemispheres. The superrotation in MAM also appears to be connected to the superrotating winds in the stratosphere, and we return to the connection between tropospheric superrotation and the QBO below. Note that the westerlies above the tropopause are not sensitive to the number of years included in the analysis, provided the time series includes enough QBO cycles; e.g., we find qualitatively similar results using 39, 40, or 41 years of data.

By contrast, the zonal winds do not exhibit tropospheric superrotation in boreal summer, and there are strong easterly winds in June–August (JJA). In both JJA and SON there is a subtropical jet in the Southern Hemisphere, though this jet is not as strong as the Northern Hemispheric subtropical jet in DJF and MAM.

Figure 2 shows the meridional and zonal variations of the equatorial zonal wind at 150 hPa, where the superrotation is strongest, as a function of month and latitude in Fig. 2a and month and longitude in Fig. 2b. The zonal mean superrotation is established in late October and reaches its peak strength in December (Fig. 2a), with a maximum speed of 4 m s^{-1}. The winds decelerate slightly in January and February, before accelerating again in March, to reach a second peak in April of around 3 m s^{-1}. Seasonal subtropical westerly jets are observed in the Northern and Southern Hemispheres, and the superrotation acts to connect the two jets when both subtropical westerly jets are present. During the rest of the year, there are strong easterly winds over the equator, associated with an easterly jet in the Northern Hemisphere. The maximum easterly equatorial wind speeds are roughly 7 m s^{-1}, stronger than the superrotating winds in other seasons, and result in the annual-mean equatorial winds being easterly [this was also noted by Zurita-Gotor (2019)]. In boreal winter there is a weak easterly jet in the Southern Hemisphere, which does not extend across the equator into the Northern Hemisphere.

Figure 2b gives a sense of the horizontal structure of the superrotation. A dipole pattern is observed in all seasons, with westerly winds over the tropical Atlantic (0°–40°W) and eastern tropical Pacific (80°W–180°), and easterly winds over the Indian Ocean and the western Pacific Ocean (40°–140°E). The westerly winds are strongest in boreal winter and spring, while the easterly winds are strongest in boreal summer, with a secondary maximum in January and February. Both the easterly and the westerly winds are weak in the spring and autumn. Hence, the seasonal superrotation seems to be related to variations in the zonal overturning circulations (Walker cells) over the tropical Atlantic and eastern Pacific, as well as to the summer monsoon circulations. However, our focus in this

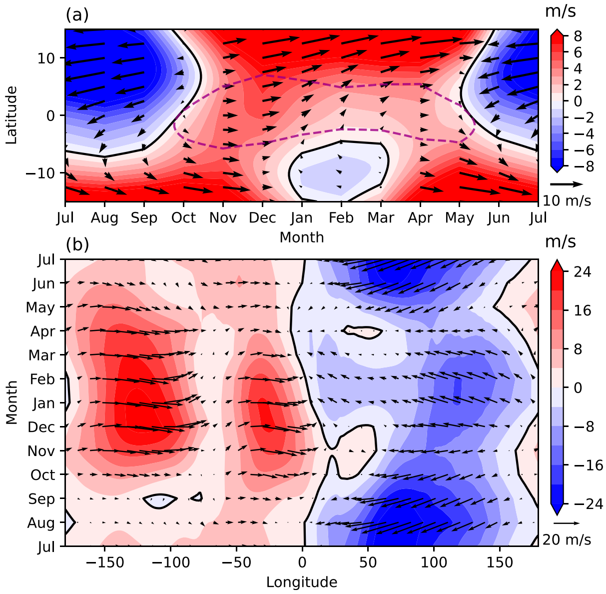

FIG. 2. Seasonality of the equatorial zonal wind speed and horizontal wind velocity direction at 150 hPa in MERRA-2: (a) the zonal mean and (b) the meridional mean between 5°S and 5°N. The shading denotes zonal wind speeds; the arrows give a sense of the strength and direction of the winds; and the contour intervals are 1 and 4 m s^{-1} in (a) and (b), respectively. Regions where the wind speed is greater than or equal to the superrotating winds defined by Eq. (1) are enclosed by the purple dashed lines in (a).

study is on the structure of the zonal-mean superrotation, and we leave the connection to regional circulations for future work.

b. *Relationships with modes of climate variability*

We now investigate the superrotation's relationships with the two primary modes of interannual variability in the tropics: ENSO and the QBO in the stratosphere.

1) ENSO

The ENSO cycle has a strong influence on tropical stationary waves, through its modulation of tropical convection (Adames and Wallace 2017). Since stationary waves are an important part of the equatorial momentum budget, we expect in turn that ENSO should have an impact on the seasonal superrotation.

Regressing the equatorial zonal-mean zonal winds at different levels and months onto the ONI shows a robust relationship between the tropospheric superrotation and ENSO (Table 2). In the first three months of superrotation (October–December, which are also the developing and mature phases of ENSO evolution), the regression coefficients are significantly negative at 150 and 200 hPa, as the superrotation tends to be stronger in La Niña years and weaker in El Niño years. There is an interesting contrast with Tziperman and Farrell (2009), who linked surface superrotation to the possible "permanent El Niño–like" Pacific in the early Pliocene, though we note that here the superrotation is confined to the upper troposphere rather than reaching down to the surface. We believe the mechanisms are likely to be quite different in the two cases.

Figure 3a further clarifies the relationship between the equatorial upper-tropospheric zonal winds and ENSO by showing the correlation coefficients between the deseasonalized monthly zonal-mean zonal wind anomalies and the ONI. Statistically significant negative correlations are seen throughout the mid- and upper troposphere (~500–125 hPa) in a narrow band of latitudes between 5°S and 5°N. Positive correlations are seen outside these latitudes, as the subtropical jets tend to shift equatorward in both hemispheres during El Niño years (Manney et al. 2021). The stratospheric winds in the deep tropics show a weak positive correlation with the ONI.

Figures 3b and 3c show the average deseasonalized zonal-mean zonal winds in strong El Niño (ONI ≥ 0.6) and strong La Niña (ONI ≤ −0.6) months, respectively. Strong El Niño months are associated with decelerations of up to −0.5 m s^{-1} in the equatorial upper troposphere, while strong La Niña months show smaller accelerations of up to 0.3 m s^{-1}. We show in the next section that the two ENSO phases produce similar magnitude anomalies in the momentum budget (see Fig. 8) despite the different strengths of the wind speed responses, suggesting either sampling error or a nonlinearity in the superrotation's response to ENSO. Interestingly, the maximum acceleration during strong La Niña events occurs at slightly lower levels than the maximum deceleration during El Niño months (~200 versus 150 hPa), which may be related to the lower tropopause height during La Niña years (Liou and Ravindra Babu 2020).

2) QBO

The westerly phase of the QBO corresponds to a state of stratospheric superrotation, which could be related to the tropospheric superrotation investigated here. Furthermore, Fig. 1 shows that the tropospheric superrotation is not well separated from the stratosphere, particularly in boreal spring. So it is possible that the two phenomena are related.

To check whether this is the case, Fig. 4a shows a Hovmöller plot of the zonal-mean zonal winds in the lower

TABLE 2. Regression coefficients of the zonal-mean zonal wind onto the ENSO index (ONI). The units are m s^{-1} K^{-1}. The first column shows the vertical level in pressure (hPa). The boldface numbers are coefficients that are statistically significant at the 95% confidence level passing a Student's *t* test.

Level (hPa)	January	February	March	April	May	June	July	August	September	October	November	December
100	**0.756**	0.102	**0.981**	**0.977**	1.140	1.080	0.364	0.062	0.143	−0.187	−0.069	−0.390
150	0.527	−0.359	−0.328	−0.944	−0.301	0.666	0.905	0.852	0.334	**−1.128**	**−1.205**	**−0.945**
200	0.146	−0.269	−0.269	−0.822	−0.287	0.525	0.733	**1.096**	0.440	**−0.962**	**−1.183**	**−0.719**

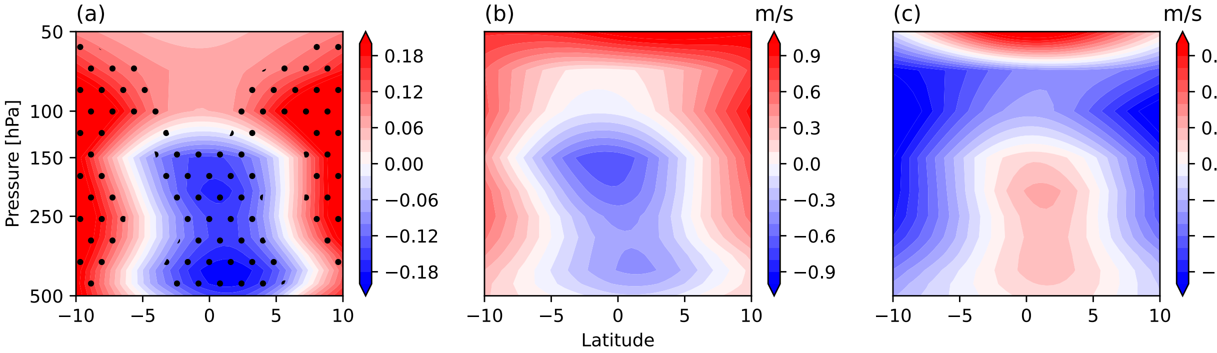

FIG. 3. (a) Correlation coefficients between the deseasonalized zonal-mean monthly zonal wind and the ONI. Stippling marks the regions where the correlation coefficients are statistically significant at the 95% confidence level, using a Student's *t* test. (b) Average of deseasonalized zonal-mean monthly zonal winds in strong El Niño months (ONI $\geq$ 0.6). (c) As in (b), but for strong La Niña months (ONI ≤ -0.6).

stratosphere and upper troposphere of the deep tropics. The quasi-biannual cycle of the QBO is clearly visible, as is the annual cycle of the tropospheric superrotation. Tropospheric superrotation can occur during the easterly (e.g., 2019), the westerly (e.g., 2018), or even the transition phase (e.g., 2015) of the QBO, suggesting that the QBO is not its primary driver. We have confirmed this by calculating the power spectra of the winds in the upper troposphere and the lower stratosphere (not shown), and find that most of the variability in the lower stratospheric is confined to a 28-month period cycle, whereas the upper-tropospheric wind's variability peaks at annual and semiannual frequencies.

Nevertheless, when we calculate the average deseasonalized equatorial zonal winds in strong positive and negative QBO phases (defined as the magnitude of the equatorial zonal wind speed at 50 hPa being greater than 10 m s^{-1}),

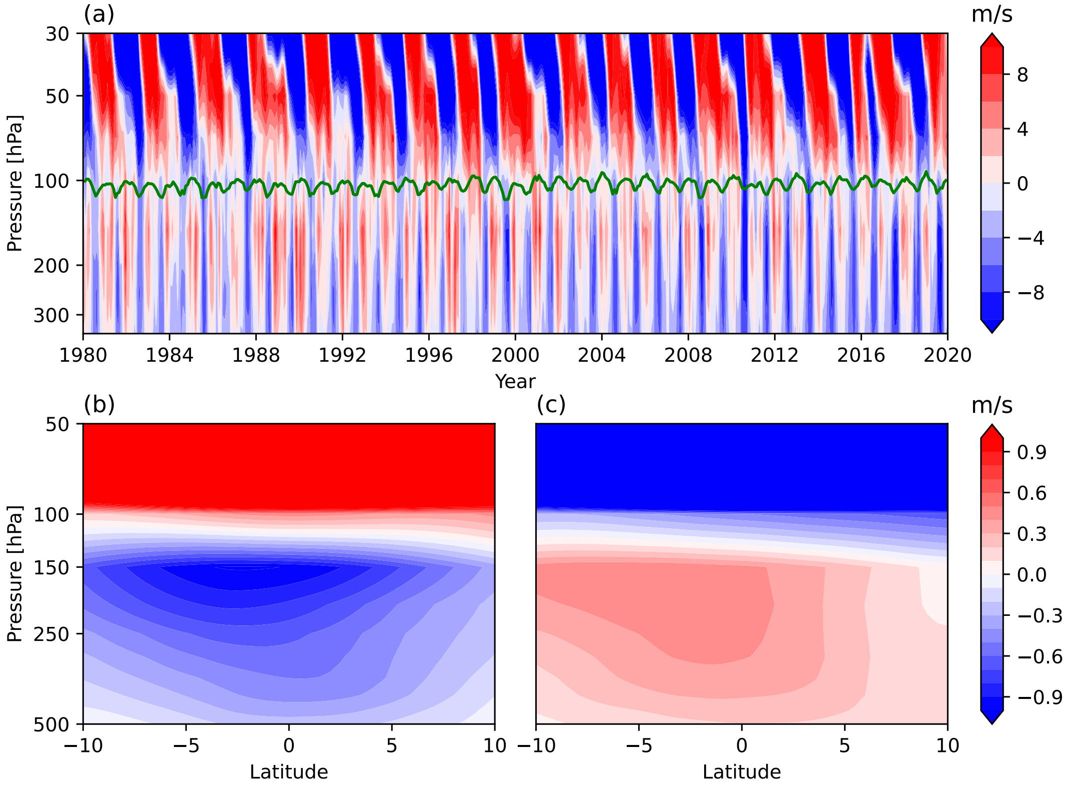

FIG. 4. (a) Zonal-mean zonal winds averaged between 5°S and 5°N in MERRA-2. The green line denotes the average height of the tropopause, calculated as in Fig. 2a. (b) Average of deseasonalized zonal-mean monthly zonal wind as in Fig. 3b, but for strong positive QBO phase [zonal wind in (a) at 50 hPa is greater than 10 m s^{-1}]. (c) As in (b), but for strong negative QBO phase [zonal wind at 50 hPa in (a) is less than -10 m s^{-1}].

TABLE 3. Linear trends of the equatorial zonal winds (second column) and of January-only, February-only, …, December-only zonal winds (rightmost 12 columns) during the period 1980–2020. The units are m s^{-1} decade^{-1}. The first column shows the vertical level in pressure (hPa). The boldface numbers are coefficients that are statistically significant at the 95% confidence level passing a Student's *t* test.

Level (hPa)	All	January	February	March	April	May	June	July	August	September	October	November	December
100	−0.109	−0.182	−0.225	0.417	0.322	0.331	**−0.862**	**−0.940**	**−0.742**	0.024	0.367	0.371	−0.259
150	**−0.721**	−0.270	−0.396	−0.441	−0.389	**−0.644**	**−1.883**	**−1.467**	**−1.881**	**−1.028**	0.211	−0.011	−0.623
200	**−0.724**	−0.302	−0.392	**−0.865**	**−0.712**	**−0.818**	**−1.834**	**−1.287**	**−1.599**	**−0.806**	0.211	0.091	−0.543

there are substantial differences (Figs. 4b,c). During the positive phase of the QBO, the averaged deseasonalized winds tend to be easterly in the upper troposphere, despite the strong westerly wind in the stratosphere; conversely, during the negative phase of QBO the deseasonalized upper-tropospheric winds tend to be westerly. The contribution of the QBO to the upper-tropospheric winds is comparable to that of ENSO in terms of magnitude and extends over a broader range of latitudes, including beyond the superrotation latitudes. To understand the sharp contrast between the stratospheric and upper-tropospheric winds in Figs. 4b and 4c, we have examined the Fourier components of these winds corresponding to a frequency of 28 months (not shown). Although most of the QBO signal dissipates before reaching the tropopause, a small part of the energy does penetrate below the tropopause and propagates downward slowly. The propagating time from 50 to 150 hPa is roughly half of the QBO period, such that the QBO's impact on the upper-tropospheric winds is out of phase with its impact on the lower-stratospheric winds. We also note that the QBO is driven by upwelling gravity waves, such that the seasonal superrotation may actually be modulating the QBO.

Despite the influence of the downwelling QBO on the tropospheric superrotation, the seasonal signal is much larger than the contribution by the QBO (or by ENSO) and produces the consistent annual cycle of the winds in the tropical upper troposphere. The variability coming from the stratosphere is overwhelmed by the intrinsic variability of tropospheric superrotation, and hence, we treat the seasonal superrotation in the upper troposphere as a distinct phenomenon from the QBO in the following discussion of its dynamics.

c. *Observed trends*

We finish characterizing the observed tropospheric superrotation by examining recent trends. Table 3 shows the linear trends of the equatorial zonal-mean zonal wind at different pressure levels. Since 1980, the annual-mean equatorial zonal winds exhibit easterly trends at 150 and 200 hPa of roughly −0.7 m s^{-1} decade^{-1}, suggesting that the superrotation has been weakening. However, when the trends are broken down by month we find that the zonal winds exhibit significant easterly trends only in boreal summer (and late spring and early autumn) months, when the winds are not superrotating.

Hence, although the equatorial zonal winds are decelerating in the annual mean, the superrotation itself has been roughly constant, except in its starting and ending months. Examining the spatial structure of the trends of monthly equatorial zonal winds further reveals that the upper troposphere is decelerating throughout the tropics, with the maximum deceleration over the equator between 150 and 200 hPa (Fig. 5). The deceleration extends over a broader range of latitudes and heights than the superrotation (see Fig. 1), suggesting that it is driven by different mechanisms.

4. The tropical zonal momentum budget

The zonal-mean zonal momentum budget of the tropical upper troposphere can be written as (Kraucunas and Hartmann 2005; Lutsko 2018)

$$\begin{aligned}\frac{\partial[\overline{u}]}{\partial t} &= f[\overline{v}] - \frac{[\overline{v}]}{a\cos\phi}\frac{\partial}{\partial\phi}([\overline{u}]\cos\phi) - [\overline{\omega}]\frac{\partial[\overline{u}]}{\partial p}\\ &\quad - \frac{1}{a\cos^2\phi}\frac{\partial}{\partial\phi}([\overline{u}^*\overline{v}^*]\cos^2\phi) - \frac{\partial}{\partial p}[\overline{u}^*\overline{\omega}^*]\\ &\quad - \frac{1}{a\cos^2\phi}\frac{\partial}{\partial\phi}([\overline{u'v'}]\cos^2\phi) - \frac{\partial}{\partial p}[\overline{u'\omega'}] + [\overline{F}_x], \qquad (7)\end{aligned}$$

where $[\cdots]$ denotes a zonal mean, $\overline{\cdots}$ denotes a temporal mean, $\cdots^*$ denotes a departure from the zonal mean, and $\cdots'$ is a departure from the temporal mean. *a* is Earth's radius, F_x is the zonal frictional drag, and *f* is the Coriolis parameter. Other notation is standard.

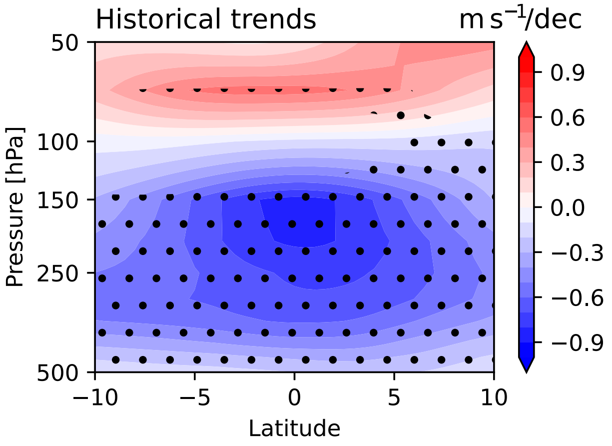

FIG. 5. Linear trends of the deseasonalized zonal-mean zonal winds over the period 1980–2020 as a function of pressure and latitude. The contour interval is 0.1 m s^{-1} decade^{-1} and stippling marks the regions where trend coefficients are statistically significant at the 95% confidence level, using a Student's *t* test.

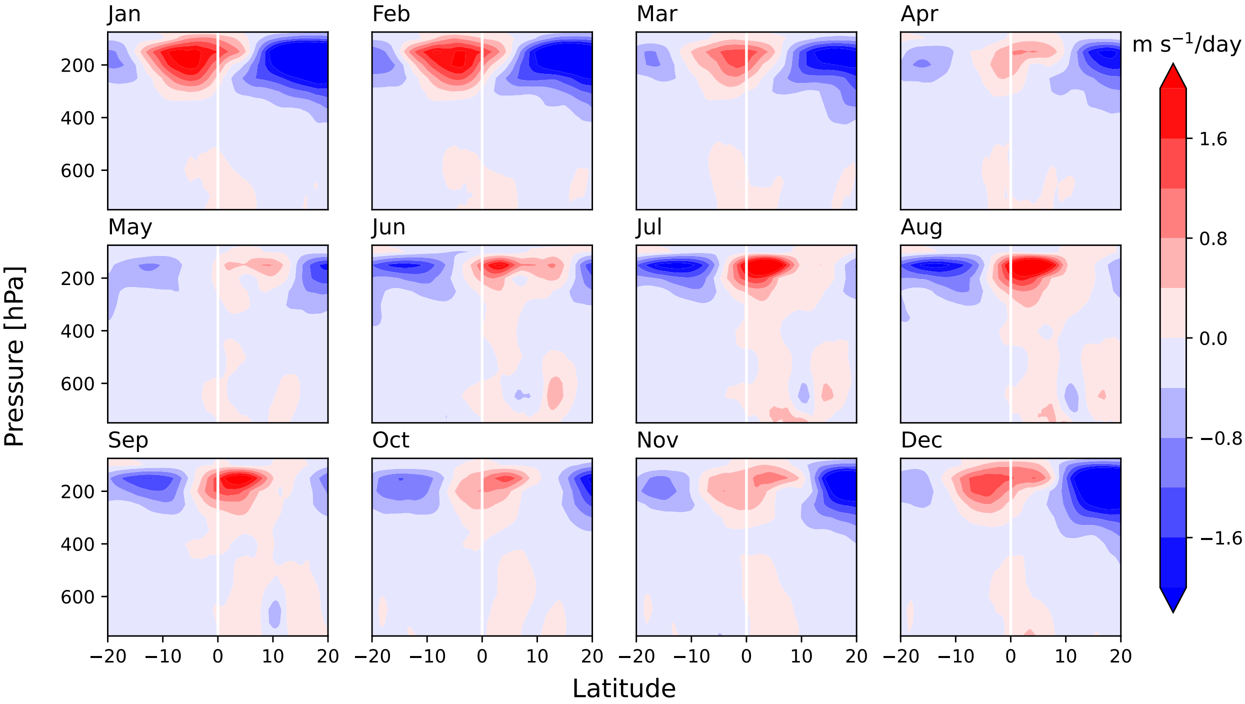

FIG. 6. Seasonal evolution of the monthly stationary horizontal term in Eq. (7) as a function of latitude and pressure. The contour interval is 0.4 m s^{-1} day^{-1} in all panels.

As in Lutsko (2018), we refer to the second and third terms on the rhs as the mean horizontal and mean vertical terms, respectively; the fourth and fifth terms as the stationary horizontal and stationary vertical terms, respectively; and the sixth and seventh terms as the transient horizontal and transient vertical terms, respectively. The frictional term is small in the free troposphere, so we have not calculated it explicitly. We have used daily mean data to calculate the momentum budget, so momentum transport by higher frequency waves is included in the residual.

a. *Monthly zonal-mean zonal momentum budgets*

To understand the dynamics of the superrotation, we have calculated the monthly-mean zonal-mean zonal momentum budget using Eq. (7). Time means represent monthly averages and transient eddies are calculated as departures from the monthly average. Each term in Eq. (7) is calculated for individual months, and the climatological monthly average is obtained to show the seasonal evolution of the terms in the budget.

The stationary horizontal term, which represents the momentum flux convergence by horizontal stationary eddies, is the only term accelerating the zonal equatorial flow (Fig. 6). This acceleration is centered at around 150 hPa, extends between roughly 300 and 100 hPa, and matches the vertical structure of the superrotation. Dima et al. (2005) also showed that the upper-tropospheric stationary waves are strongest near the 150 hPa level, consistent with the vertical position of superrotation. Further away from the equator, there are two regions of deceleration by stationary waves in each hemisphere. This is analogous to the momentum transport at midlatitudes, where Rossby waves transport momentum from wave sinks to sources (Thompson 1971; Hide and Mason 1975; Held 1975), and suggests the presence of wave sources close to the equator. One likely driver of tropical stationary waves is deep convection, for example in the Indo-Pacific warm pool. This convection is part of the Walker circulation, and both the superrotation and the Walker circulation are stronger in La Niña than in El Niño years. We will come back to ENSO’s influence on the momentum budget later in this section.

The location of the maximum acceleration by the stationary horizontal term varies over the course of the year, from just north of the equator in boreal summer to just south of the equator in boreal winter. This shift corresponds to the north–south migration of the ITCZ, and suggests the stationary wave source shifts with the ITCZ. The strength of the acceleration shows a semiannual cycle: the acceleration is largest in boreal winter, then decays until its contribution in the deep tropics is negligible in May; in the boreal summer another peak is observed, and then the stationary horizontal acceleration decays again in the autumn. The winter peak of the eddy momentum flux convergence coincides with the period of superrotation but, unlike the superrotation, the stationary horizontal term also peaks in boreal summer. The boreal summer peak is weaker than the boreal winter peak.

Off the equator, the two regions of deceleration by stationary waves also exhibit an annual cycle, with the deceleration stronger in the winter hemisphere than in the summer hemisphere, consistent with Kraucunas and Hartmann (2005).

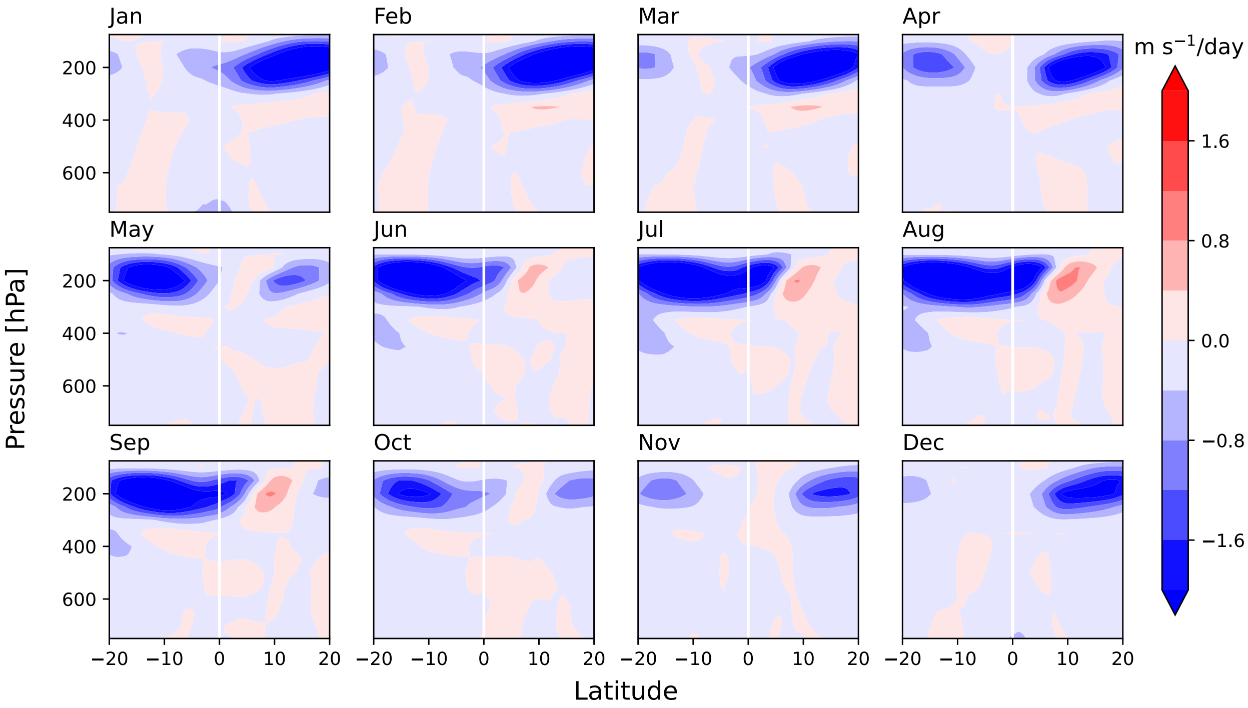

FIG. 7. Seasonal cycle of the monthly mean horizontal term in Eq. (7) as a function of latitude and pressure. The contour interval is 0.4 m s^{-1} day^{-1} in all panels.

Moreover, the winter deceleration in the subtropics is stronger in DJF (boreal winter) than in JJA (austral winter), which matches the finding of Schneider and Bordoni (2008) that the winter overturning cell in boreal summer is angular momentum conserving, whereas in DJF the winter cell is primarily eddy dominated.

The major deceleration of equatorial flow is induced by the mean horizontal term. In the monthly budget, this term represents the transport of air with low angular momentum across the equator by the mean meridional flow associated with the seasonal Hadley cells. The importance of deceleration by the mean flow is consistent with Lee (1999) and Dima et al. (2005), who concluded that the most significant factor stopping the tropics from superrotating in the annual mean is the "transient" meridional circulation associated with the seasonal cycles of the Hadley cells, though the transience of the Hadley cells in their studies is categorized as a mean flow effect in our monthly budget. Mitchell et al. (2014) also showed that even a relatively weak seasonal cycle effectively prevents model atmospheres from developing superrotation.

Figure 7 shows the annual cycle of the mean horizontal term. The deceleration is strongest in boreal winter and summer when the cross-equatorial meridional flow is strong, and weakest in spring and autumn when the Hadley cells are roughly symmetric and the cross-equatorial flow is weak. The strong deceleration in boreal summer—even stronger than in boreal winter—explains why the winds do not superrotate in that season despite the substantial acceleration by stationary eddies. This is consistent with the differing strength of the winter Hadley cells: stronger in austral winter than in boreal winter, reflecting the northward displacement of ITCZ from the equator in the annual mean. We will further discuss the effect of the displaced annual-mean ITCZ in section 5.

Together, the mean horizontal term and the mean stationary term largely explain the superrotation,[4] and more generally, the seasonal evolution of the upper-tropospheric winds in the tropics (see also Zurita-Gotor 2019). Other terms in the momentum budget, such as the vertical terms and transient horizontal term, play minor roles in the monthly momentum budget of the deep tropics (see Fig. B1 in appendix B), though they may be important in other contexts [e.g., the vertical momentum flux can be crucial when superrotation becomes much stronger, as in Kraucunas and Hartmann (2005), for example].

Putting these results together shows that superrotation of the upper troposphere can only develop outside the boreal summer months, when the deceleration by the mean flow is relatively weak and cannot overcome the acceleration by the stationary waves. Even in autumn and spring, when the stationary momentum convergence is weak, the mean flow deceleration is unable to inhibit the superrotation. But in boreal summer, the strong cross-equatorial flow decelerates the zonal-mean winds so strongly that in the annual mean the zonal-mean winds are easterly.

---

[4] Note that these two terms may not be fully decoupled or independent. E.g., Shaw (2014) investigated stationary waves' impact on the seasonal transition of general circulation.

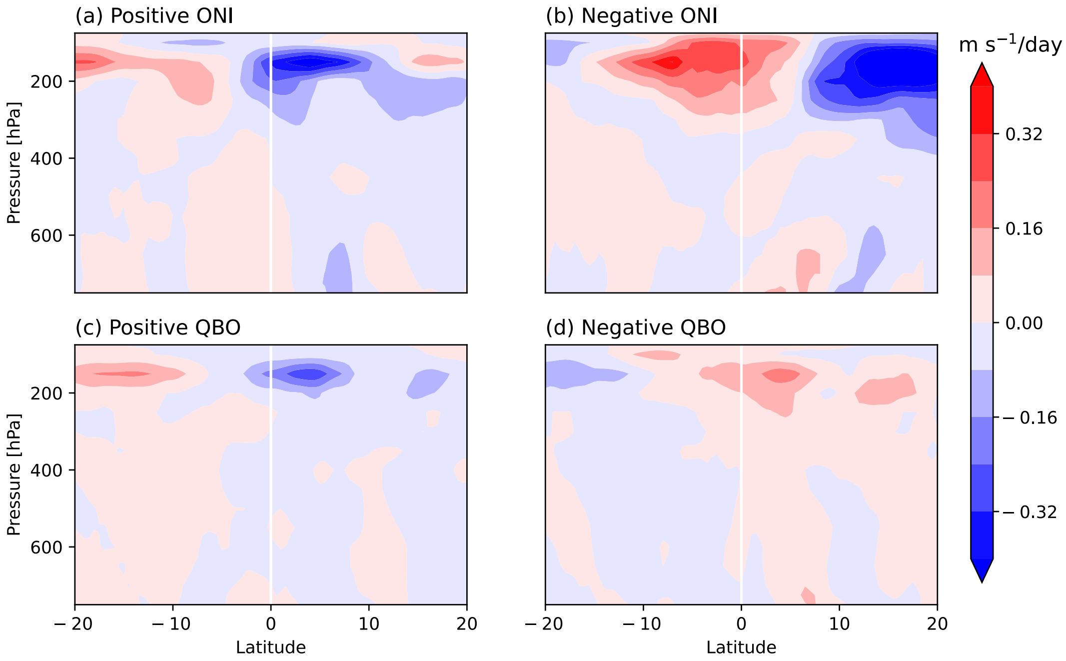

FIG. 8. (top) Anomalous monthly stationary horizontal term, (a) in strong El Niño months (ONI ≥ 0.6), and (b) in strong La Niña months (ONI ≤ −0.6). (bottom) As in the top row, but for (c) positive QBO months (equatorial zonal-mean zonal wind is greater than 10 m s^{-1}) and (d) negative QBO months (equatorial zonal-mean zonal wind is less than −10 m s^{-1}).

b. *Influences of ENSO and QBO*

In section 3, the ENSO and the QBO were shown to have notable influences on the strength of superrotation, which suggests that they impact the stationary eddy momentum convergence that drives the superrotation. To explore this possibility, we have averaged the anomalous monthly stationary horizontal term (deviations from the climatological monthly mean) over strong El Niño months (ONI ≥ 0.6, 111 months) and strong La Niña months (ONI ≤ −0.6, 107 months), as well as over strong positive and negative QBO months (Fig. 8, 161 and 119 months, respectively). Note that other terms, such as the mean horizontal and vertical terms, are weakly correlated to ENSO and to the QBO (not shown), suggesting that both modes of variability primarily influence the momentum budget through changes in stationary waves.

For ENSO, the anomalous stationary horizontal term is negative over the equator between 300 and 100 hPa during strong El Niño months and positive during strong La Niña months (Figs. 8a,b), as the momentum convergence by stationary eddies becomes weaker in El Niño years and stronger in La Niña years.[5] This explains why the superrotation is stronger in La Niña years and weaker in El Niño years, though, interestingly, the magnitude of the anomalous stationary horizontal term is similar during El Niño and La Niña months, whereas the wind response is stronger during El Niño than La Niña (Fig. 3). This could be the result of sampling bias or of a nonlinear mechanism by which ENSO modifies the superrotation.

The QBO modifies the equatorial momentum convergence in the region of superrotation in a similar manner to ENSO (Figs. 8c,d). Note that the anomalies are stronger in positive QBO than in negative QBO phases, consistent with the differing strengths of the wind responses to QBO phases (Fig. 4). We have not investigated the stationary wave response to the QBO further, but note that Yang et al. (2012) found that the upper-tropospheric planetary waves over the eastern Pacific region appear to be stronger during the easterly phase, and Collimore et al. (2003) and Yamazaki et al. (2020) also suggested that the easterly phase enhances deep convection in the tropical western Pacific. Investigating the couplings between the QBO, the winds of the tropical upper troposphere and tropical stationary waves, all of which modify and are modified by each other, could be a fruitful topic of future research.

5. Understanding the superrotation with an idealized model

The previous section showed how stationary momentum flux convergence and deceleration by the mean flow combine to produce the observed seasonal cycle of winds in the

---

[5] See Adames and Wallace (2017) for a discussion of how stationary waves change over the course of the ENSO cycle; Dima and Wallace (2007) and Grise and Thompson (2012) also suggested enhanced amplitudes of the equatorial planetary waves associated with “La Niña–like” SST anomalies, which are perhaps induced by modulation of tropical convection.

tropical upper troposphere. The northward-displaced ITCZ also appears to play a role in setting the seasonal cycle of the superrotation. We now use an axisymmetric single-layer model to further understand the dynamics and seasonal development of the superrotation. We also verify our arguments from the momentum budget analysis, and separately show the effects of the stationary eddy momentum flux convergence and the displacement of the ITCZ.

We consider four model configurations: 1) no eddy momentum flux divergence [EMFD; $\mathscr{S}$ in Eq. (2)] and hemispherically symmetric insolation, 2) no EMFD but hemispherically asymmetric insolation, 3) prescribed EMFD and hemispherically symmetric insolation, and 4) prescribed EMFD and hemispherically asymmetric insolation. The purpose of hemispherically asymmetric insolation is to match the observed northward displacement of the ITCZ in the annual mean. The prescribed EMFD is based on the stationary horizontal terms described in the previous section, and takes the following form:

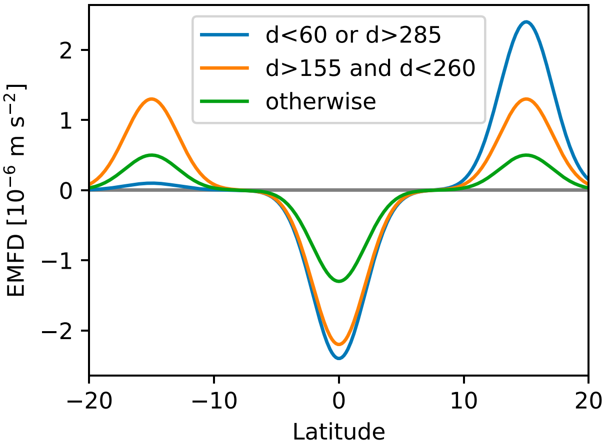

FIG. 9. Prescribed eddy momentum flux divergence in the model simulations, based on the stationary horizontal term.

$$\mathscr{S} = \begin{cases} -2.4N(0,3) + 2.4N(15,3) + 0.1N(-15,3) & \text{if } d < 60 \text{ or } d > 285, \\ -2.2N(0,3) + 1.3N(15,3) + 1.3N(-15,3) & \text{if } d > 155 \text{ and } d < 260, \\ -1.3N(0,3) + 0.5N(15,3) + 0.5N(-15,3) & \text{otherwise}, \end{cases} \tag{8}$$

where the units are 10^{-6} m s^{-1}, d is the day of the year, ranging from 0 to 364, and $N(0, 3)$ is a Gaussian function centered at 0° with a maximum of 1 and a standard deviation of $3°/\sqrt{2}$. $\mathscr{S}$ is shown in Fig. 9.

This function captures the key features of the horizontal stationary term in the upper troposphere: 1) peaks in boreal summer and winter; 2) weak, hemispherically symmetric EMFD in the shoulder seasons; and 3) strong subtropical deceleration in the Northern Hemisphere during boreal winter. Our formulation of $\mathscr{S}$ roughly matches the observed EMFD, but allows more freedom to adjust the parameters and match the observations. Given the idealizations of the model and the difficulty of constraining certain model parameters such as friction, we find it easier to prescribe an EMFD that can be tuned so that the model matches the observations. Moreover, the simulation results, in terms of the key feature of superrotation, are qualitatively robust to the choice of $\mathscr{S}$ (not shown).

With this numerical model, we are able to clarify how the northward displacement of the ITCZ and the stationary eddy momentum convergence contribute to the seasonal superrotation. We begin with the simplest case of an ITCZ that is symmetric about the equator and with no eddy momentum convergence input. Figure 10c and the blue curve in Fig. 10a show that in this case the winds in the equatorial upper troposphere are easterly in all seasons. The easterly flow is driven by the easterly momentum transport by the cross-equatorial mean flow of the upper branch of the Hadley cell, which gives a semiannual cycle in the upper-tropospheric winds. The easterly winds are weakest in spring and autumn when the ITCZ is close to the equator and the cross-equatorial flow is weak; hence, these seasons are most favorable for the development of superrotation.

In the second simulation the annual mean ITCZ is displaced to the Northern Hemisphere (Fig. 10d and the orange curve in Fig. 10a). In this case the equatorial wind has an annual rather than a semiannual cycle, as the easterlies substantially strengthen in boreal summer and weaken in boreal winter, breaking the symmetry between summer and winter. This is because the cross-equatorial flow is stronger in boreal summer, when the ITCZ is further from the equator, than in winter, when the ITCZ is closer. A stronger easterly flow is expected for an angular-momentum conserving Hadley circulation that is displaced off the equator in the annual mean (Lindzen and Hou 1988).

Next, we add eddy momentum flux convergence to the model. This accelerates the flow, and drives seasonal superrotation when the cross-equatorial flow is weak in the shoulder seasons (Figs. 10e,f, and the green and red curves in Fig. 10a). The resulting superrotation has either an annual cycle or a semiannual cycle, depending on the mean ITCZ position. In the hemispherically symmetric case (Fig. 10e and green curve in Fig. 10a), the superrotation peaks in boreal spring and autumn with almost equal strength, and completely disappears in boreal summer and winter. In the displaced ITCZ case (Fig. 10f and red curve in Fig. 10a), the annual-mean zonal flow is decelerated because of the stronger easterlies in boreal summer. This is partially compensated by slower easterlies in boreal summer and stronger superrotation in the shoulder seasons. The time between the two westerly peaks is shortened by several months, and the upper-tropospheric winds exhibit a roughly annual cycle.

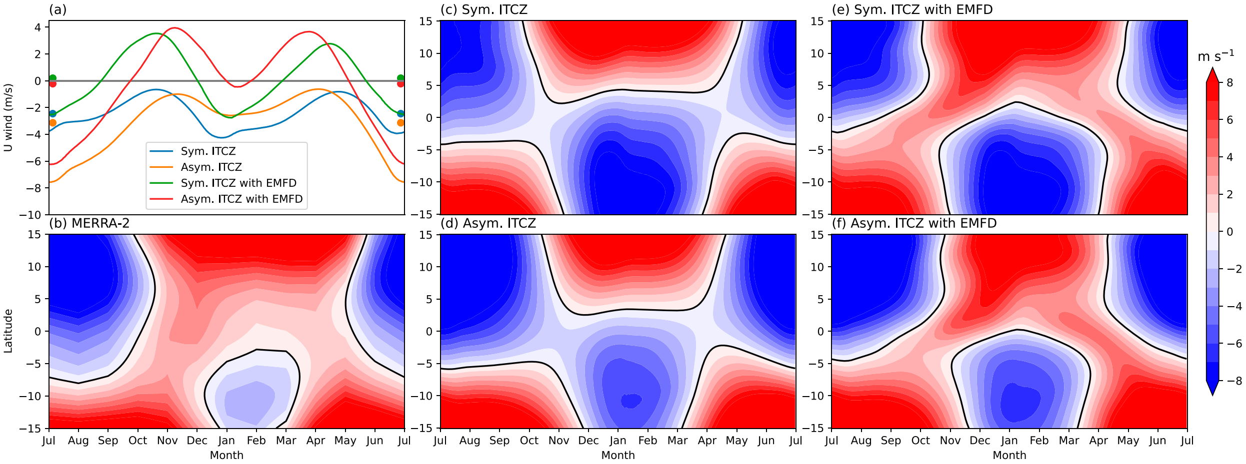

FIG. 10. (a) The equatorial wind from the numerical model under different model configurations; winds are averaged between 3°S and 3°N and the colored dots on the y axis show the annual mean winds in each configuration. (b) The seasonality of the equatorial winds in MERRA-2, averaged between 100 and 200 hPa. (c)–(f) Seasonality and latitudinal distribution of the equatorial wind in the numerical model simulations: (c) symmetric ITCZ, (d) northward-displaced ITCZ, (e) symmetric ITCZ with prescribed EMFD, and (f) northward-displaced ITCZ with prescribed EMFD. The contour interval is 1 m s^{-1} in (b)–(f).

The model simulation with prescribed EMFD and a displaced annual-mean ITCZ shows good agreement with the MERRA-2 data (Figs. 10b,f). Just like the reanalysis data, the superrotation starts in October and reaches a first peak of ~4 m s^{-1} in late November. In boreal winter the superrotation decays to zero, then reaches a second peak in late March, which has almost the same strength as the first one. Finally the superrotation vanishes in late May, and after that the equatorial upper troposphere is dominated by strong easterly winds, with a maximum of more than 6 m s^{-1}. As for the spatial structure, the superrotation extends the subtropical easterly jet toward the equator, as we see in Figs. 10b and 1. The subtropical easterlies are caused by the Coriolis force acting on the mean meridional flow in the winter hemisphere, although the driver of superrotation itself is not the Coriolis force. All these features are consistent with what is observed in MERRA-2 (Fig. 10b or Fig. 2a).

There are still some differences between the model output and MERRA-2. For example, the easterly wind is stronger in boreal winter and the overall amplitude of the wind is slightly higher in the model. This likely reflects the simplifications of the model, and we have also not rigorously tuned the model, so it may be possible to produce an even better fit to the data. Nevertheless, the model successfully captures the main features of the superrotation and provides several insights into its dynamics. First, the model simulations confirm that momentum transport by the meridional flow associated with the seasonal Hadley cells decelerates the upper-tropospheric winds and prevents superrotation in the annual mean (see also Lee 1999; Dima et al. 2005). The model also illustrates how this effect can be interpreted in terms of the annual-mean ITCZ being displaced off the equator. Second, the momentum convergence induced by eddies accelerates the atmosphere to reach a superrotating state when the deceleration by the meridional flow is weak in boreal winter, autumn and spring. Finally, the asymmetric ITCZ not only slows down the annual mean equatorial wind, but also breaks the temporal symmetry of the seasonal superrotation, giving it an annual, rather than semiannual, cycle.

6. Conclusions

In this study, we have characterized the seasonal superrotation of Earth's tropical upper troposphere using MERRA-2 data. We have described the structure and seasonal evolution of the superrotation, and also identified the drivers of the superrotation using the monthly zonal-mean zonal momentum budget of the tropics. A single-layer axisymmetric model is then used to study how stationary eddy momentum fluxes and the northward displacement of the annual-mean ITCZ combine to determine the superrotation's strength and annual cycle.

The tropospheric superrotation is centered at 150 hPa and has a clear annual cycle: it is established in October, reaches peaks in December and in March, and vanishes in late April. The maximum westerlies can reach up to 4 m s^{-1} during the first peak in December. The equatorial upper troposphere exhibits strong easterly winds in boreal summer, such that the tropical upper troposphere does not superrotate in the annual mean. Regressions onto the ENSO index show that the superrotation tends to be stronger in boreal winter during La Niña years, and weaker during El Niño years, while the relationship with the QBO is complex. The tropospheric superrotation is clearly a distinct phenomenon from the stratospheric superrotation during the westerly phase of the QBO, but the superrotation is actually strengthened during the easterly phase of the QBO, when the westerly acceleration of the previous (westerly) QBO phase appears to descend into the upper troposphere. On the other hand, since the QBO is driven by

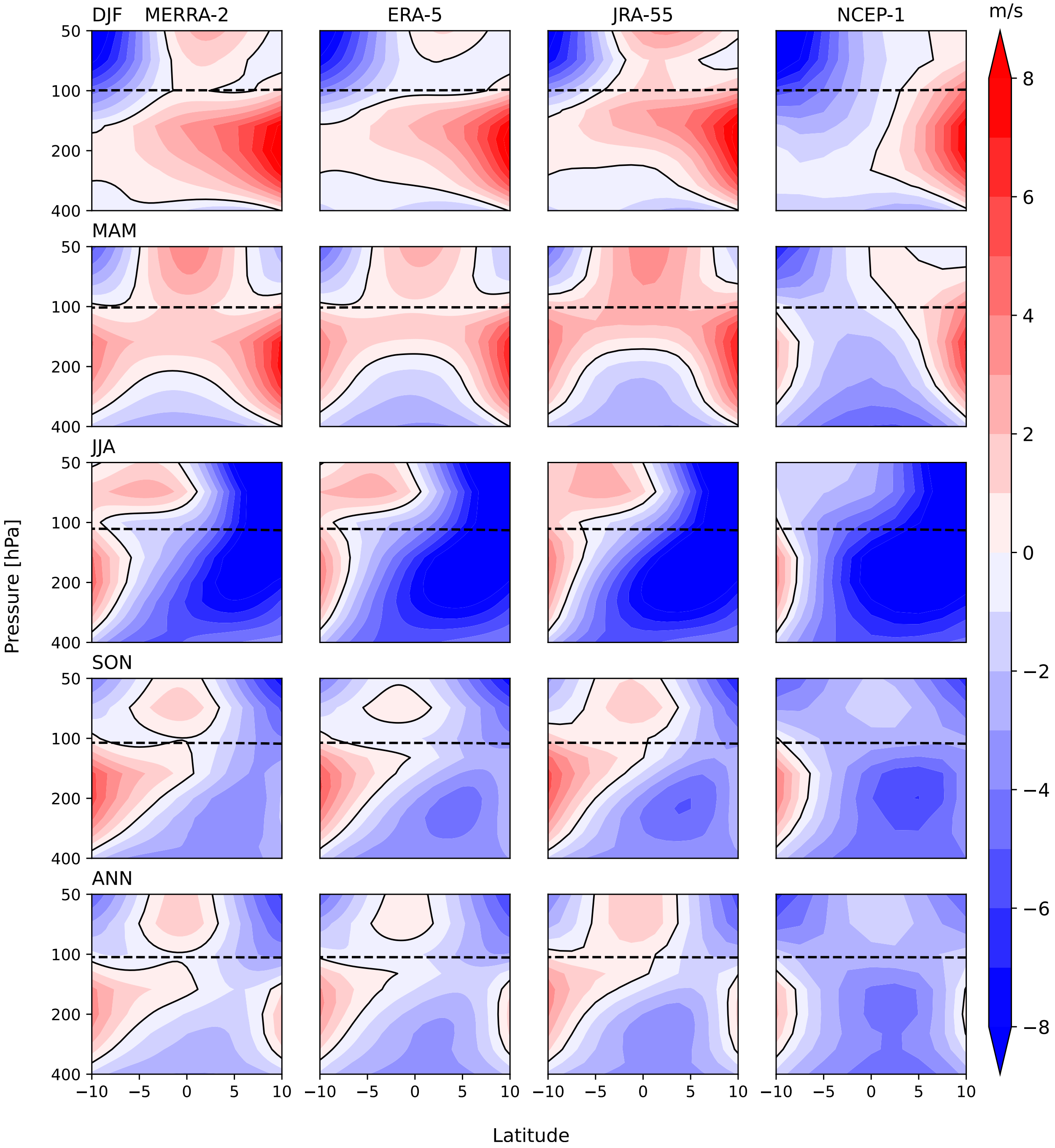

FIG. A1. Seasonality of the tropical zonal-mean zonal wind speeds at different latitudes and levels in different reanalysis products: (from left to right) MERRA-2, ERA5, JRA-55, and NCEP-1, respectively. Five rows correspond to (from top to bottom) DJF, MAM, JJA, SON, and annual mean, respectively. The shading denotes wind velocities, with a contour interval 1 m s^{-1}. The black dashed lines denote the average height of the tropopause, defined as the lowest level at which the lapse rate decreases to 2 K km^{-1} or less.

upwelling gravity waves, the direction of causality is ambiguous. On longer time scales, there was a negative trend in the annual-mean winds of the upper troposphere over the period 1980–2020, but the trends were negligible from October to March, so that the strength of the superrotation has been roughly constant over the past few decades.

The zonal momentum budget analysis and numerical model simulations have provided insights into the dynamics of the tropospheric superrotation. Consistent with Dima et al. (2005) and Zurita-Gotor (2019), the dominant balance in the momentum equation on monthly time scales is between momentum flux convergence by stationary eddies and easterly momentum

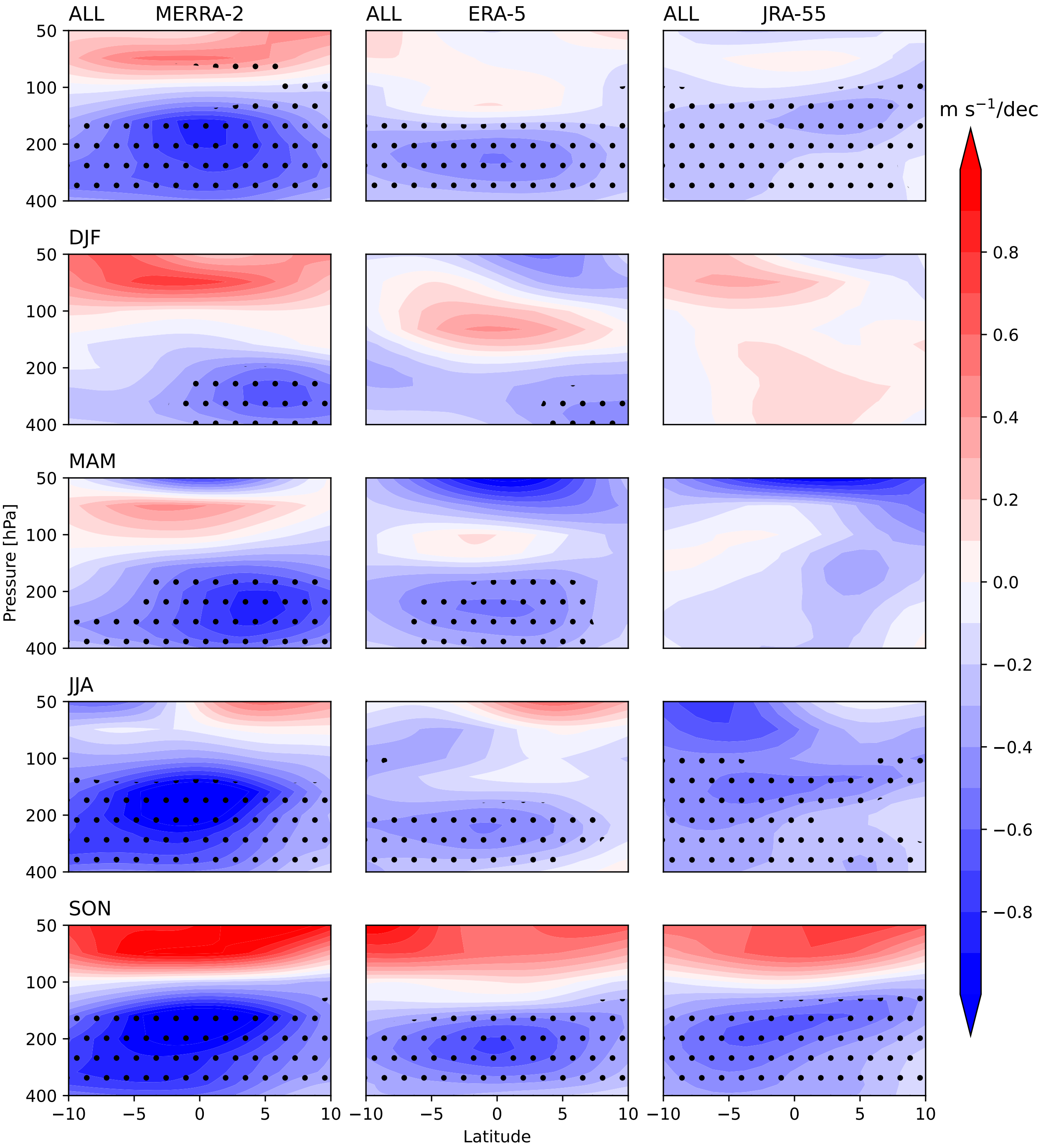

FIG. A2. Linear trends of (first row) the deseasonalized monthly zonal winds and (second to fifth rows) DJF-only, MAM-only, JJA-only, and SON-only zonal winds during the period 1980–2020 as a function of pressure and latitude in different reanalysis products: (left) MERRA-2, (center) ERA5, and (right) JRA-55. The contour interval is 0.1 m s^{-1} decade^{-1} and stippling marks the regions where trend coefficients are statistically significant at the 95% confidence level, using a Student's *t* test.

transport by the cross-equatorial mean flow of the Hadley circulation, with the former accelerating and the latter decelerating the upper troposphere. The stationary eddy momentum flux convergence is strongest in boreal winter and summer, whereas the deceleration by the mean flow is strongest in boreal summer, which is what prevents the tropical troposphere from superrotating in boreal summer and causes the winds to be easterly in the annual mean. Lee (1999) included the seasonal cycle of the Hadley circulation in the transient term of the annual-mean momentum budget, and similarly identified this term as the main factor stopping annual-mean superrotation.

The numerical model further reinforced the importance of the stationary eddy momentum convergence for driving the superrotation; without this acceleration, the winds of the tropical upper troposphere would be easterly throughout the year. The model also revealed the importance of the northward displacement of the ITCZ in the annual mean for determining the seasonal cycle of the superrotation. If the annual-mean ITCZ was symmetric about the equator the winds of the tropical upper troposphere would exhibit a semiannual cycle, with periods of strong superrotation in boreal spring and autumn, and easterly winds in boreal summer and winter. Instead, the winds exhibit an annual cycle, because the deceleration by the mean flow is relatively weak in boreal winter. Even in simulations without eddy forcing, a transition between semiannual and annual cycles is seen depending on the ITCZ's annual-mean position. Finally, we may infer that, if Earth were to have lower obliquity, or if the annual-mean ITCZ were closer to the equator, the winds of the tropical upper troposphere would likely superrotate in the annual mean.

Our focus in this study has been on the zonal-mean structure and dynamics of the superrotation. We have not attempted to characterize the structure of the stationary waves which drive the superrotation (see Zurita-Gotor 2019), nor how these waves change during the ENSO and QBO cycles. Figure 2b further suggests that the superrotation is related to changes in the zonal overturning cells in the deep tropics (the Walker cell, etc.), and clarifying this relationship is another topic for future research. More work is also needed to investigate how the seasonal superrotation relates to intraseasonal modes of tropical variability, such as the Madden–Julian oscillation (e.g., see Caballero and Huber 2010), as well as to examine climate model projections of how the superrotation will change in the future.

Acknowledgments. The manuscript was much improved by constructive comments and feedback from Professor Jun Yang and two other anonymous reviewers. We thank Matt Luongo, Professor Shang-Ping Xie, and Professor Pablo Zurita-Gotor for helpful comments on earlier versions of this manuscript.

Data availability statement. The MERRA-2 data are available at Goddard Earth Sciences Data and Information Services Center (GES DISC; https://doi.org/10.5067/QBZ6MG944HW0). The ERA5 data are available at Copernicus Climate Data Store (https://doi.org/10.24381/cds.6860a573). The JRA-55 data are available at GES DISC (https://doi.org/10.5065/D60G3H5B). The NCEP-1 data are available on NOAA's website (https://psl.noaa.gov/data/gridded/data.ncep.reanalysis.html). The ONI index is available on CPC website (https://origin.cpc.ncep.noaa.gov/products/analysis_monitoring/ensostuff/ONI_v5.php). The numerical model used in section 5 is publicly available at https://github.com/zpcllyj/SobelSchneiderModel.

APPENDIX A

Seasonal Superrotation in Other Reanalysis Products

To verify the robustness of the seasonal superrotation, Fig. A1 shows the zonal-mean zonal winds in the deep tropics of four reanalysis products: MERRA-2, ERA5, JRA-55, and NCEP-1. The first three reanalysis products show close agreement in terms of the spatial and temporal structure of the winds, despite minor differences in wind speed magnitude, but NCEP-1 does not exhibit superrotation in boreal winter (rightmost column in Fig. A1), consistent with Dima et al. (2005). We have not investigated what causes the differences in NCEP-1, but note that in addition to being an older dataset, the horizontal resolution of NCEP-1 is only 2.5° × 2.5°, much lower than the resolutions of the three other modern reanalysis products. This lower resolution could lead to a worse representation of tropical waves, which might impact the representation of the seasonal cycle of the tropical winds.

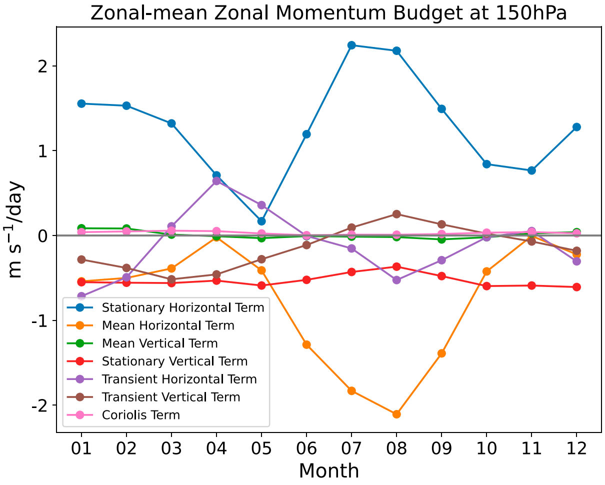

FIG. B1. Seasonal evolution of terms in Eq. (7) at 150 hPa and averaged between 3°S and 3°N. The friction and tendency terms are not shown.

We have also used the different reanalysis products to verify our claim that the superrotation did not exhibit meaningful trends over the period of study (1980–2020). Figure A2 shows the linear trends of the winds in the tropical upper troposphere in the three high-resolution reanalysis products: MERRA-2, ERA5, and JRA-55. None of the datasets show a statistically significant trend in DJF, when the superrotation is most pronounced, though the trends are very different in the three datasets. The trends are more consistent in the annual mean, with a negative trend in the middle troposphere, but the magnitude and position are slightly different. This trend appears to be driven by a different mechanism than the superrotation, as the maximum deceleration is below the superrotation level and the trend is generally strongest in boreal summer, when superrotation is absent.

APPENDIX B

Other Terms in the Momentum Budget

To justify our statement that the stationary and mean horizontal terms are the key factors shaping the dynamics of the seasonal superrotation, in Fig. B1 we show the seasonal cycles of the terms in the zonal-mean zonal momentum budget [Eq. (7)] at 150 hPa. All terms are averaged between 3°S and 3°N, and we ignore the friction and tendency terms. The stationary and mean horizontal terms dominate the momentum budget for most of the year, and their features are as discussed in section 4. The other terms are either negligible or lack significant seasonal variations, and hence are of secondary importance for the seasonal superrotation. Nevertheless, the effects of these secondary terms on the equatorial momentum budget and on the superrotation could be an interesting topic of future research.

REFERENCES

Adames, A. F., and J. M. Wallace, 2017: On the tropical atmospheric signature of El Niño. *J. Atmos. Sci.*, **74**, 1923–1939, https://doi.org/10.1175/JAS-D-16-0309.1.

Arnold, N. P., E. Tziperman, and B. Farrell, 2012: Abrupt transition to strong superrotation driven by equatorial wave resonance in an idealized GCM. *J. Atmos. Sci.*, **69**, 626–640, https://doi.org/10.1175/JAS-D-11-0136.1.

Baldwin, M. P., and Coauthors, 2001: The quasi-biennial oscillation. *Rev. Geophys.*, **39**, 179–229, https://doi.org/10.1029/1999RG000073.

Belton, M. J. S., and Coauthors, 1991: Images from Galileo of the Venus cloud deck. *Science*, **253**, 1531–1536, https://doi.org/10.1126/science.253.5027.1531.

Bird, M. K., and Coauthors, 2005: The vertical profile of winds on Titan. *Nature*, **438**, 800–802, https://doi.org/10.1038/nature04060.

Caballero, R., and M. Huber, 2010: Spontaneous transition to superrotation in warm climates simulated by CAM3. *Geophys. Res. Lett.*, **37**, L11701, https://doi.org/10.1029/2010GL043468.

Collimore, C. C., D. W. Martin, M. H. Hitchman, A. Huesmann, and D. E. Waliser, 2003: On the relationship between the QBO and tropical deep convection. *J. Climate*, **16**, 2552–2568, https://doi.org/10.1175/1520-0442(2003)016<2552:OTRBTQ>2.0.CO;2.

Dahlman, L., 2016: Climate variability: Oceanic Niño index. NOAA, https://www.climate.gov/news-features/understanding-climate/climate-variability-oceanic-nino-index.

Dima, I. M., and J. M. Wallace, 2007: Structure of the annual-mean equatorial planetary waves in the ERA-40 reanalyses. *J. Atmos. Sci.*, **64**, 2862–2880, https://doi.org/10.1175/JAS3985.1.

——, ——, and I. Kraucunas, 2005: Tropical zonal momentum balance in the NCEP reanalyses. *J. Atmos. Sci.*, **62**, 2499–2513, https://doi.org/10.1175/JAS3486.1.

Eliassen, A., and E. Kleinschmidt, 1957: Dynamic meteorology. *Handbuch der Physik*, Vol. 48, Springer, 64–72.

Gelaro, R., and Coauthors, 2017: The Modern-Era Retrospective Analysis for Research and Applications, version 2 (MERRA-2). *J. Climate*, **30**, 5419–5454, https://doi.org/10.1175/JCLI-D-16-0758.1.

Genio, A. D. D., R. K. Achterberg, K. H. Baines, F. M. Flasar, P. L. Read, A. Sánchez-Lavega, and A. P. Showman, 2009: Saturn atmospheric structure and dynamics. *Saturn from Cassini-Huygens*, M. K. Dougherty, L. W. Esposito, and S. M. Krimigis, Eds., Springer, 113–159.

Gierasch, P. J., 1975: Meridional circulation and the maintenance of the Venus atmospheric rotation. *J. Atmos. Sci.*, **32**, 1038–1044, https://doi.org/10.1175/1520-0469(1975)032<1038:MCATMO>2.0.CO;2.

Gill, A. E., 1980: Some simple solutions for heat-induced tropical circulation. *Quart. J. Roy. Meteor. Soc.*, **106**, 447–462, https://doi.org/10.1002/qj.49710644905.

GMAO, 2015: MERRA-2 inst3_3d_asm_Np: 3d, 3-hourly, instantaneous, pressure-level, assimilation, assimilated meteorological fields version 5.12.4. GES DISC, accessed September 2021, https://doi.org/10.5067/QBZ6MG944HW0.

Grise, K. M., and D. W. J. Thompson, 2012: Equatorial planetary waves and their signature in atmospheric variability. *J. Atmos. Sci.*, **69**, 857–874, https://doi.org/10.1175/JAS-D-11-0123.1.

Held, I. M., 1975: Momentum transport by quasi-geostrophic eddies. *J. Atmos. Sci.*, **32**, 1494–1497, https://doi.org/10.1175/1520-0469(1975)032<1494:MTBQGE>2.0.CO;2.

——, and A. Y. Hou, 1980: Nonlinear axially symmetric circulations in a nearly inviscid atmosphere. *J. Atmos. Sci.*, **37**, 515–533, https://doi.org/10.1175/1520-0469(1980)037<0515:NASCIA>2.0.CO;2.

Herbert, C., R. Caballero, and F. Bouchet, 2020: Atmospheric bistability and abrupt transitions to superrotation: Wave–jet resonance and Hadley cell feedbacks. *J. Atmos. Sci.*, **77**, 31–49, https://doi.org/10.1175/JAS-D-19-0089.1.

Hersbach, H., and Coauthors, 2020: The ERA5 global reanalysis. *Quart. J. Roy. Meteor. Soc.*, **146**, 1999–2049, https://doi.org/10.1002/qj.3803.

Hide, R., 1969: Dynamics of the atmospheres of the major planets with an appendix on the viscous boundary layer at the rigid bounding surface of an electrically-conducting rotating fluid in the presence of a magnetic field. *J. Atmos. Sci.*, **26**, 841–853, https://doi.org/10.1175/1520-0469(1969)026<0841:DOTAOT>2.0.CO;2.

——, 1970: Equatorial jets in planetary atmospheres. *Nature*, **225**, 254–255, https://doi.org/10.1038/225254b0.

——, and P. Mason, 1975: Sloping convection in a rotating fluid. *Adv. Phys.*, **24**, 47–100, https://doi.org/10.1080/00018737500101371.

Hill, S. A., S. Bordoni, and J. L. Mitchell, 2019: Axisymmetric constraints on cross-equatorial Hadley cell extent. *J. Atmos. Sci.*, **76**, 1547–1564, https://doi.org/10.1175/JAS-D-18-0306.1.

Horinouchi, T., and Coauthors, 2020: How waves and turbulence maintain the super-rotation of Venus' atmosphere. *Science*, **368**, 405–409, https://doi.org/10.1126/science.aaz4439.

Hoskins, B., R. Neale, M. Rodwell, and G.-Y. Yang, 1999: Aspects of the large-scale tropical atmospheric circulation. *Tellus*, **51A**, 33–44, https://doi.org/10.3402/tellusa.v51i1.12287.

Kalnay, E., and Coauthors, 1996: The NCEP/NCAR 40-Year Reanalysis Project. *Bull. Amer. Meteor. Soc.*, **77**, 437–472, https://doi.org/10.1175/1520-0477(1996)077<0437:TNYRP>2.0.CO;2.

Kobayashi, S., and Coauthors, 2015: The JRA-55 reanalysis: General specifications and basic characteristics. *J. Meteor. Soc. Japan*, **93**, 5–48, https://doi.org/10.2151/jmsj.2015-001.

Kostiuk, T., and Coauthors, 2006: Stratospheric global winds on Titan at the time of Huygens descent. *J. Geophys. Res.*, **111**, E07S03, https://doi.org/10.1029/2005JE002630.

Kraucunas, I., and D. L. Hartmann, 2005: Equatorial superrotation and the factors controlling the zonal-mean zonal winds in the tropical upper troposphere. *J. Atmos. Sci.*, **62**, 371–389, https://doi.org/10.1175/JAS-3365.1.

Laraia, A. L., and T. Schneider, 2015: Superrotation in terrestrial atmospheres. *J. Atmos. Sci.*, **72**, 4281–4296, https://doi.org/10.1175/JAS-D-15-0030.1.

Lee, S., 1999: Why are the climatological zonal winds easterly in the equatorial upper troposphere? *J. Atmos. Sci.*, **56**, 1353–1363, https://doi.org/10.1175/1520-0469(1999)056<1353:WATCZW>2.0.CO;2.

Lewis, N. T., G. J. Colyer, and P. L. Read, 2021: Characterizing regimes of atmospheric circulation in terms of their global superrotation. *J. Atmos. Sci.*, **78**, 1245–1258, https://doi.org/10.1175/JAS-D-20-0326.1.

Lindzen, R. S., and A. V. Hou, 1988: Hadley circulations for zonally averaged heating centered off the equator. *J. Atmos. Sci.*, **45**, 2416–2427, https://doi.org/10.1175/1520-0469(1988)045<2416:HCFZAH>2.0.CO;2.

Liou, Y.-A., and S. Ravindra Babu, 2020: ENSO signatures observed in tropical tropopause layer parameters using long-term COSMIC RO data. *GPS Solutions*, **24**, 98, https://doi.org/10.1007/s10291-020-01009-7.

Lutsko, N. J., 2018: The response of an idealized atmosphere to localized tropical heating: Superrotation and the breakdown of linear theory. *J. Atmos. Sci.*, **75**, 3–20, https://doi.org/10.1175/JAS-D-17-0192.1.

Manney, G. L., M. I. Hegglin, and Z. D. Lawrence, 2021: Seasonal and regional signatures of ENSO in upper tropospheric jet characteristics from reanalyses. *J. Climate*, **34**, 9181–9200, https://doi.org/10.1175/JCLI-D-20-0947.1.

Matsuno, T., 1966: Quasi-geostrophic motions in the equatorial area. *J. Meteor. Soc. Japan*, **44**, 25–43, https://doi.org/10.2151/jmsj1965.44.1_25.

Mitchell, J. L., and G. K. Vallis, 2010: The transition to superrotation in terrestrial atmospheres. *J. Geophys. Res.*, **115**, E12008, https://doi.org/10.1029/2010JE003587.

——, ——, and S. F. Potter, 2014: Effects of the seasonal cycle on superrotation in planetary atmospheres. *Astrophys. J.*, **787**, 23, https://doi.org/10.1088/0004-637X/787/1/23.

NOAA, 2020: Four El Niño regions. NOAA, accessed September 2020, https://www.cpc.ncep.noaa.gov/products/analysis_monitoring/ensostuff/nino_regions.shtml.

——, 2021: Cold and warm episodes by season. NOAA, accessed September 2021, https://origin.cpc.ncep.noaa.gov/products/analysis_monitoring/ensostuff/ONI_v5.php.

Norton, W. A., 2006: Tropical wave driving of the annual cycle in tropical tropopause temperatures. Part II: Model results. *J. Atmos. Sci.*, **63**, 1420–1431, https://doi.org/10.1175/JAS3698.1.

Peralta, J., R. Hueso, and A. Sánchez-Lavega, 2007: A reanalysis of Venus winds at two cloud levels from Galileo SSI images. *Icarus*, **190**, 469–477, https://doi.org/10.1016/j.icarus.2007.03.028.

Pierrehumbert, R. T., and M. Hammond, 2019: Atmospheric circulation of tide-locked exoplanets. *Annu. Rev. Fluid Mech.*, **51**, 275–303, https://doi.org/10.1146/annurev-fluid-010518-040516.

Pinto, J. R. D., and J. L. Mitchell, 2016: Wave–mean flow interactions and the maintenance of superrotation in a terrestrial atmosphere. *J. Atmos. Sci.*, **73**, 3181–3196, https://doi.org/10.1175/JAS-D-15-0208.1.

Polichtchouk, I., and J. Y.-K. Cho, 2016: Equatorial superrotation in Held and Suarez like flows with weak equator-to-pole surface temperature gradient. *Quart. J. Roy. Meteor. Soc.*, **142**, 1528–1540, https://doi.org/10.1002/qj.2755.

Potter, S. F., G. K. Vallis, and J. L. Mitchell, 2014: Spontaneous superrotation and the role of Kelvin waves in an idealized dry GCM. *J. Atmos. Sci.*, **71**, 596–614, https://doi.org/10.1175/JAS-D-13-0150.1.

Sakai, S., 1989: Rossby-Kelvin instability: A new type of ageostrophic instability caused by a resonance between Rossby waves and gravity waves. *J. Fluid Mech.*, **202**, 149–176, https://doi.org/10.1017/S0022112089001138.

Saravanan, R., 1993: Equatorial superrotation and maintenance of the general circulation in two-level models. *J. Atmos. Sci.*, **50**, 1211–1227, https://doi.org/10.1175/1520-0469(1993)050<1211:ESAMOT>2.0.CO;2.

Schneider, T., 2006: The general circulation of the atmosphere. *Annu. Rev. Earth Planet. Sci.*, **34**, 655–688, https://doi.org/10.1146/annurev.earth.34.031405.125144.

——, and S. Bordoni, 2008: Eddy-mediated regime transitions in the seasonal cycle of a Hadley circulation and implications for monsoon dynamics. *J. Atmos. Sci.*, **65**, 915–934, https://doi.org/10.1175/2007JAS2415.1.

Seiff, A., 2000: Dynamics of Jupiter's atmosphere. *Nature*, **403**, 603–605, https://doi.org/10.1038/35001171.

Shaw, T. A., 2014: On the role of planetary-scale waves in the abrupt seasonal transition of the Northern Hemisphere general circulation. *J. Atmos. Sci.*, **71**, 1724–1746, https://doi.org/10.1175/JAS-D-13-0137.1.

Showman, A. P., and L. M. Polvani, 2010: The Matsuno-Gill model and equatorial superrotation. *Geophys. Res. Lett.*, **37**, L18811, https://doi.org/10.1029/2010GL044343.

——, and ——, 2011: Equatorial superrotation on tidally locked exoplanets. *Astrophys. J.*, **738**, 71, https://doi.org/10.1088/0004-637X/738/1/71.

Sobel, A. H., and T. Schneider, 2009: Single-layer axisymmetric model for a Hadley circulation with parameterized eddy momentum forcing. *J. Adv. Model. Earth Syst.*, **1** (3), https://doi.org/10.3894/JAMES.2009.1.10.

——, and ——, 2013: Correction to "Single-layer axisymmetric model for a Hadley circulation with parameterized eddy momentum forcing." *J. Adv. Model. Earth Syst.*, **5**, 654–657, https://doi.org/10.1002/jame.20030.

Suarez, M. J., and D. G. Duffy, 1992: Terrestrial superrotation: A bifurcation of the general circulation. *J. Atmos. Sci.*, **49**, 1541–1554, https://doi.org/10.1175/1520-0469(1992)049<1541:TSABOT>2.0.CO;2.

Thompson, R. O. R. Y., 1971: Why there is an intense eastward current in the North Atlantic but not in the South Atlantic. *J. Phys. Oceanogr.*, **1**, 235–237, https://doi.org/10.1175/1520-0485(1971)001<0235:WTIAIE>2.0.CO;2.

Tsai, S.-M., I. Dobbs-Dixon, and P.-G. Gu, 2014: Three-dimensional structures of equatorial waves and the resulting super-rotation in the atmosphere of a tidally locked hot Jupiter. *Astrophys. J.*, **793**, 141, https://doi.org/10.1088/0004-637X/793/2/141.

Tziperman, E., and B. Farrell, 2009: Pliocene equatorial temperature: Lessons from atmospheric superrotation. *Paleoceanography*, **24**, PA1101, https://doi.org/10.1029/2008PA001652.

Wang, P., and J. L. Mitchell, 2014: Planetary ageostrophic instability leads to superrotation. *Geophys. Res. Lett.*, **41**, 4118–4126, https://doi.org/10.1002/2014GL060345.

Williams, G. P., 2003: Barotropic instability and equatorial superrotation. *J. Atmos. Sci.*, **60**, 2136–2152, https://doi.org/10.1175/1520-0469(2003)060<2136:BIAES>2.0.CO;2.

Yamazaki, K., T. Nakamura, J. Ukita, and K. Hoshi, 2020: A tropospheric pathway of the stratospheric quasi-biennial oscillation (QBO) impact on the boreal winter polar vortex. *Atmos. Chem. Phys.*, **20**, 5111–5127, https://doi.org/10.5194/acp-20-5111-2020.

Yang, G.-Y., B. Hoskins, and L. Gray, 2012: The influence of the QBO on the propagation of equatorial waves into the stratosphere. *J. Atmos. Sci.*, **69**, 2959–2982, https://doi.org/10.1175/JAS-D-11-0342.1.

Yang, W., R. Seager, and M. A. Cane, 2013: Zonal momentum balance in the tropical atmospheric circulation during the global monsoon mature months. *J. Atmos. Sci.*, **70**, 583–599, https://doi.org/10.1175/JAS-D-12-0140.1.

Zurita-Gotor, P., 2019: The role of the divergent circulation for large-scale eddy momentum transport in the tropics. Part I: Observations. *J. Atmos. Sci.*, **76**, 1125–1144, https://doi.org/10.1175/JAS-D-18-0297.1.

——, and I. M. Held, 2018: The finite-amplitude evolution of mixed Kelvin–Rossby wave instability and equatorial superrotation in a shallow-water model and an idealized GCM. *J. Atmos. Sci.*, **75**, 2299–2316, https://doi.org/10.1175/JAS-D-17-0386.1.

——, A. Anaya-Benlliure, and I. M. Held, 2022: The sensitivity of superrotation to the latitude of baroclinic forcing in a terrestrial dry dynamical core. *J. Atmos. Sci.*, **79**, 1311–1323, https://doi.org/10.1175/JAS-D-21-0269.1.